Numerical investigation of nanofluid deposition in a microchannel cooling system

Meng Wang [a,b], Phillip S. Dobson [b], Manosh C. Paul [a,*]

[a] *Systems, Power & Energy Research Division, James Watt School of Engineering, University of Glasgow, Glasgow G12 8QQ, UK*
[b] *Electronics & Nanoscale Engineering Division, James Watt School of Engineering, University of Glasgow, Glasgow G12 8QQ, UK*

HIGHLIGHTS

- Liquid-based nanoparticle deposition in a microchannel was studied.
- Optimal flow characteristics were obtained to reduce deposition.
- Ideal nanofluid properties were selected to delay deposition.
- Deposition effect was evaluated by heat transfer and pressure drop comprehensively.

GRAPHICAL ABSTRACT
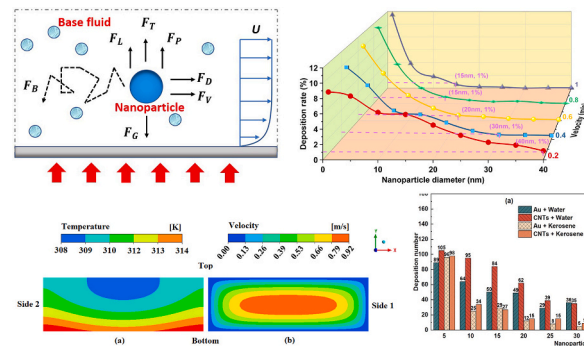
ARTICLE INFO

ABSTRACT

Nanofluid-microchannels (NF-MCs) have emerged as an important topic for thermal management of electronic devices. However, deposition of nanoparticles is a tricky problem, and this paper conducts a numerical study to identify the best working conditions to prevent deposition of nanofluids in a microchannel cooling system. According to the findings, large nanoparticles, high velocity, low inlet temperature, high nanoparticle density, low nanofluid density, and high base fluid viscosity are the best working conditions for improving nanofluid stability. However, heat transfer rates and pressure drop must also be taken into account. The nanoparticle deposition rate and average heat transfer coefficient only increase by 2.71% and 0.92% respectively as the heat flux increases from 20 kW/m^2 to 100 kW/m^2, but the pressure drop decreases by 10.57%. Therefore, changing the heat flux is not the best option. Moreover, the inlet temperature has only a minor effect on the heat transfer coefficient, so it is crucial to balance the pressure drop and nanoparticle deposition when designing systems.

1. Introduction

At present, conventional working fluids used in microelectronic cooling systems cannot meet the increased heat dissipation requirements of these devices. Thus, Choi et al. [1] investigated the thermal properties of nanofluids composed of well-dispersed nanoparticle suspensions [2]. Nanofluids have many advantages, including adjustable properties, high thermal conductivity and high specific surface area [3]. Dehghan et al. simulated Al$_2$O$_3$-water nanofluids in

---

Nomenclature

R_i	Richardson number		Nu	Nusselt number
g	gravitational acceleration		*Greeks*	
l	characteristic length		β	thermal expansion coefficient
v	velocity		ρ	density
$\overrightarrow{F}$	external body forces		$\overline{\tau}$	stress tensor
P	static pressure		μ	dynamic viscosity
I	unit tensor		ν	kinematic viscosity
T	temperature		λ	mean free path
k	thermal conductivity		φ	volume concentration
C_p	specific heat		*Acronyms*	
S_T	volumetric heat sources		NF-MC	nanofluid-microchannel
h	heat transfer coefficient		MCHS	microchannel heat sink
m	mass		DPM	discrete phase model
ζ_i	Gaussian white noise function		CFD	computational fluid dynamics
Δt	time step			
S_0	spectral intensity		*Subscripts*	
k_B	Boltzmann constant		*hot*	hot wall
C_c	Cunningham correction		*ref*	reference
Kn	Knudsen number		p	particle
d_p	nanoparticle diameter		B	Brownian force
D_T	thermophoretic diffusion coefficient		T	thermophoretic force
C_{vm}	virtual mass factor		G	Gravity
τ_r	particle relaxation time		V	virtual mass force
Re_r	relative Reynolds number		D	drag force
K	Saffman number		P	pressure gradient force
d_{ij}	deformation tensor		L	Saffman's lift force
N	deposition particle number		nf	nanofluids
			bf	base fluid

converging flow passages, showing that the nanofluid enhanced the convection heat transfer coefficient [4]. Additionally, Wen and Ding [5] concluded that nanofluids enhanced heat transfer, particularly at the entrance area. Whereas Esfe et al. [6] reported that the increase in heat transfer coefficient was primarily due to a change in the thermal conductivity of pure water and nanofluids with nanoparticle concentrations of 0.0625%, 0.125%, 0.25%, 0.5%, and 1%. In addition, different applications of nanofluids are reported in solar systems, industrial processes and biomedical fields. The study by Aljaloud et al. [7] focused on the thermal impact of cross nanofluid with applications of bioconvection phenomenon and found that the velocity profile increased as the curvature index and curvature parameter increased. Huhemandula et al. [8] simulated Graphene Oxide-water nanofluid in a solar collector heat exchanger to predict the whole range of data. Although nanofluids have been researched for around 20 years, it is still challenging to employ them on an industrial scale. There are three primary reasons: firstly, it is difficult to manufacture a number of nanofluids; secondly, nanofluids have a narrow operating range, and cannot be used at their boiling point; finally, nanoparticles can be quickly deposited out of their base fluids so losing the characteristics and advantages of nanofluids [9]. The third reason is the most severe problem, so this paper focuses on nanoparticle deposition.

Nanofluids are suspensions of nanoparticles in base fluids. Different nanoparticles and base fluids are used to synthesize different thermophysical properties of a fluid. The most common nanoparticles are copper, aluminium, gold and nickel [10]. Various carbon materials including carbon nanotubes (CNTs), multiwall carbon nanotubes (MWCNTs), diamonds, and graphite also provide nanofluids with enhanced thermophysical properties. However, metallic nanoparticles and carbon materials lack widespread industrial application because of their high cost [11]. Consequently, alternative materials are more commonly used, including metal oxide (Al_2O_3, CuO, MgO, ZnO, SiO_2, Fe_2O_3, TiO_2), metal nitride (AlN, Si_3N_4), and metal carbide (SiC, TiC). As

for the base fluid, water, ethylene glycol, methanol, kerosene, and transformer oil are all commonly used.

In a parallel line of research, Tuckerman and Pease first introduced the concept of MCHS at Stanford University in the early 1980s [12]. Since MCHS have the advantage of large heat transfer surfaces to volume ratios, compact structures, and outstanding thermal performance, they have been primarily applied to heat dissipation of electronic devices with high heat flux [13–15]. Most researchers improved thermal efficiency by changing the channel structure. For instance, Dehghan et al. [16] found that the pumping power of an MCHS using converging flow passages could be reduced by a factor of four compared to that of a straight channel at the same heat dissipation rate. Wang et al. [17] found that rectangular microchannel has better thermal performance than trapezoid and triangle microchannels, hence the rectangular microchannels used in this paper. However, clogging can be a problem because of its compact structure, resulting in reduced performance and lifespan.

A combination of nanofluids and MCHS is an effective method to improve MCHS thermal performance [18]. However, a nanoparticle diameter of 1 to 100 nm and the hydraulic diameter of the microchannel of 10 to 200 μm create deposition and clogging problems. In this scenario, nanofluids lose their high-efficiency characteristics due to deposition, while MCHS see reduced heat transfer, increased energy consumption, and a shorter lifespan [19–21]. Nanofluid stability is being improved through chemical approaches. By studying static nanofluids, researchers analysed the underlying reason for these problems [22,23]. Consequently, one way to achieve stable nanofluids is through the addition of surfactants, balancing their surface charges [24,25]. At the same time, mechanical mixing or ultrasonication is another effective method for reducing agglomeration [26–28], which continuously breaks the bonds between particles. Nevertheless, stationary nanofluids are far from industrial applications. These systems require flowing fluid, and there have only been a few studies examining

the thermal factors that influence the deposition of flowing nanofluids [29]. Therefore, this paper investigates the factors that influence the deposition of flowing nanofluids.

As a result of the accumulation of deposition nanoparticles in applications, fouling occurs. Deposition is a tricky problem in modern nanomaterial applications. Water treatment systems, for example, are especially vulnerable to membrane fouling as it affects desalination and reclamation efficiency [30,31]. Fouling in food production systems also adversely affects the organoleptic quality of the product and reduces production [32,33]. Fouling in biological systems results in arterial blood flow blockage. On the other hand, fouling can also occur in internal channels [19–21] and outside fins [34] of heat transfer devices, such as heat exchangers. Nanofluid-microchannel heat exchangers prevent fouling by prolonging or preventing particle deposition. The number of published papers in this area is relatively small, and most researchers have paid considerable attention to the effects of particle migration on heat transfer efficiency. According to the study of Goudarzi et al. [35], particle migration significantly increased the Nusselt number by increasing thermophoresis diffusion by up to 11%. As for the research of Hedayati and Domairry [36], local conductivity and viscosity increased in regions with high nanoparticle concentrations, resulting in stronger conduction and weaker convection rates. Particle migration reduces heat transfer, and particle deposition destroys the entire system. Therefore, a better method of stopping particle deposition should be researched.

To apply nanofluid cooling technology widely, the deposition problem in NF-MC systems must be resolved. Nanoparticle stability has been studied extensively, but most studies focused on chemical methods for improving stability in static fluids. In real systems, flow characteristics and properties also affect nanoparticle stability, so recently, researchers have begun to investigate the deposition of gas-based fluids [37,38]. However, there are almost no studies conducted on liquid-based fluids (nanofluids) and the nanoparticles moving in microchannels. Therefore, a discrete phase model (DPM) is used to simulate the nanofluid properties (i.e., nanoparticle diameter, nanoparticle density, base-fluid density, and base-fluid viscosity) and the flow characteristics (i.e., velocity, heat flux, and inlet temperature). Furthermore, heat transfer performance and pressure drop are also considered for each working condition. Overall, this paper aims to find the optimal working conditions to prolong nanoparticle deposition in nanofluids and provides a comprehensive evaluation of each working condition, which benefits the design of NF-MC cooling systems.

2. Numerical modelling and methods

As shown in Fig. 1, a 3D microchannel model is created with a width of 0.2 mm and a height of 0.067 mm. The channel length is 20 mm, which is sufficient for a fully developed flow under the flow Reynolds number investigated. The mass continuity, momentum, and energy transport equations are simultaneously solved using Computational Fluid Dynamics (CFD), ANSYS Fluent 2020 *Ra*. The Euler-Lagrange approach, regarding dispersed phases as dispersions, is applied on nanofluids. So, DPM is employed in this study since the nanoparticle concentration is consider to be <10% [37]. In DPM, the base fluid is considered as a continuum fluid phase, solved by the Navier-Stokes equations, and the nanoparticles are regarded as dispersions, calculated from the flow field. To improve the precision and efficiency of the calculation, the following assumptions are made:

(1) Nanofluid flow is three-dimensional, steady and incompressible.
(2) Nanoparticles are smooth and spherical.
(3) The volume concentration of nanoparticles is <10%, so the interactions between the nanoparticles are ignored [38].
(4) A one-way coupling method is applied. So, the base fluid affects nanoparticles, while the influence of the nanoparticles on the base flow is neglected [39].
(5) The distribution of nanoparticles is uniform in the inlet.
(6) According to Eq. (1), Richardson number $R_i = 3.99 \times 10^{-4} < 0.1$, so forced convection is dominant in this study.

$$Ri = \frac{g\beta(T_{hot} - T_{ref})l}{v^2} \quad (1)$$

where g is the gravitational acceleration, β is the thermal expansion coefficient, T_{hot} is the hot wall temperature, T_{ref} is the reference temperature, l is the characteristic length, and v is the fluid velocity.

2.1. Flow field simulation

The governing equations of the developing fluid flow in microchannel are presented below.

Mass continuity equation:

$$\nabla \cdot (\rho \overrightarrow{v}) = 0 \quad (2)$$

Momentum conservation equation:

$$\nabla \cdot (\rho \overrightarrow{v} \overrightarrow{v}) = -\nabla P + \nabla \cdot (\overline{\tau}) + \rho \overrightarrow{g} + \overrightarrow{F} \quad (3)$$

Where $\overline{\tau}$ is the stress tensor defined as:

$$\overline{\tau} = \mu \left[(\nabla \overrightarrow{v} + \nabla \overrightarrow{v}^T) - \frac{2}{3} \nabla \cdot \overrightarrow{v} I \right] \quad (4)$$

Energy transport equation:

$$\nabla \cdot (\rho T \overrightarrow{v}) = \nabla \cdot \left(\frac{k}{C_p} grad\ T \right) + S_T \quad (5)$$

where ρ is the density; $\overrightarrow{v}$ is the velocity vector; P is the static pressure; $\overrightarrow{F}$
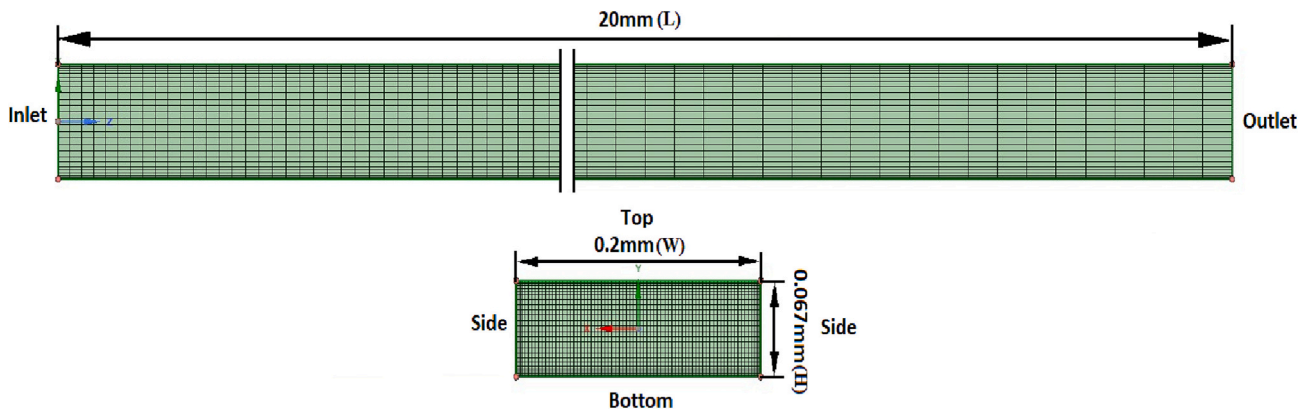

Fig. 1. Schematic of the calculation domain and meshing of a MCHS.

is the external body forces (for example, that arise from the interaction with the dispersed phase); $\rho \vec{g}$ is the gravitational body force; μ is the dynamic viscosity; T is the temperature; I is the unit tensor; k is the thermal conductivity; C_p is the specific heat; and S_T is the source term.

The presence of particles changes the energy equation in Eq. (5) as they pass through each of the control volumes in the simulation. Thus, the energy transfer between particles and base fluid is calculated as [40]:

$$S_T = \sum_{np} \frac{m_p}{\delta V} C_{p,p} \cdot \frac{dT_p}{dt} \tag{6}$$

where C_p is the specific heat capacity; δV is the number of particles within a cell volume and the cell with $np = 0$ is assigned a zero value for S_T. The shape of the particle is spherical in the simulation, so the energy equation of a particle is obtained as [40,41]:

$$\rho_p C_{p,p} \frac{dT_p}{dt} = \frac{6h}{d_p} (T - T_p) \tag{7}$$

where h is the heat transfer coefficient.

2.2. Particle transport simulation

The forces of nanoparticle transport mainly include Brownian motion, thermophoretic force, Gravity, virtual mass force, drag force, pressure gradient force and Saffman's lift force. Therefore, the nanoparticle trace is calculated by the Newton's Second Law of motion [42]:

$$m_p \frac{d\vec{v_p}}{dt} = \vec{F_B} + \vec{F_T} + \vec{F_G} + \vec{F_V} + \vec{F_D} + \vec{F_P} + \vec{F_L} \tag{8}$$

where m_p is the nanoparticle mass; and $\vec{v_p}$ is the nanoparticle velocity.

The amplitude of the Brownian force components F_{B_i} is expressed as [43,44]:

$$F_{B_i} = m_p \zeta_i \sqrt{\frac{\pi S_o}{\Delta t}} \tag{9}$$

where ζ_i is the Gaussian white noise function with a zero-mean value; Δt is the time step; and S_0 is a spectral intensity defined as:

$$S_0 = \frac{216 \nu k_B T}{\pi^2 \rho d_p^5 \left(\frac{\rho_p}{\rho}\right)^2 C_c} \tag{10}$$

where C_c is the Cunningham correction (i.e., slip correction factor) that modifies the slip condition on the nanoparticle surface defined as [45]:

$$C_c = 1 + Kn\left(1.257 + 0.4 exp\left(-\frac{1.1}{Kn}\right)\right) \tag{11}$$

where $Kn = 2\lambda/d_p$ is the Knudsen number; ν is the kinematic viscosity; k_B is the Boltzmann constant 1.3807×10^{-23} J/K; d_p is the nanoparticle diameter; and λ is the mean free path.

The thermophoretic force is formulated as [46]:

$$\vec{F_T} = -D_T \frac{\nabla T}{T} \tag{12}$$

where ∇T is the temperature difference; and D_T is the thermophoretic diffusion coefficient determined as:

$$D_T = \frac{6\pi d_p \mu^2 C_s (K + C_t Kn)}{\rho (1 + 3C_m Kn)(1 + 2K + 2C_t Kn)} \tag{13}$$

Where $K = k/k_p$; k_p is the nanoparticle thermal conductivity; and for a spherical nanoparticle shape, C_s=1.17, C_t=2.18, C_m=1.14 [46].

The Gravitational force component is calculated by:

$$\vec{F_G} = m_p \frac{\vec{g} (\rho_p - \rho_l)}{\rho_p} \tag{14}$$

The virtual mass force is calculated as [42]:

$$\vec{F_V} = C_{vm} m_p \frac{\rho}{\rho_p} \left(\vec{v_p} \nabla \vec{v} - \frac{d\vec{v_p}}{dt}\right) \tag{15}$$

where C_{vm} is the virtual mass factor. For nanofluids, the distance between nanoparticles is far due to low concentration, therefore $C_{vm} = 0.5$ [47].

The drag force is related to the fluid friction, which is determined by [48]:

$$\vec{F_D} = m_p \frac{\vec{v} - \vec{v_p}}{\tau_r} \tag{16}$$

where τ_r is the nanoparticle relaxation time defined as:

$$\tau_r = \frac{\rho_p d_p^2}{18\mu} \frac{24}{C_c Re_r} \tag{17}$$

where Re_r is the relative Reynolds number given by:

$$Re_r = \frac{\rho d_p |\vec{v} - \vec{v_p}|}{\mu} \tag{18}$$

The pressure gradient force is shown by [42]:

$$\vec{F_P} = m_p \frac{\rho}{\rho_p} \vec{v_p} \nabla \vec{v} \tag{19}$$

Finally, the Saffman's lift force is induced by the slip-shear velocity between fluid and nanoparticle, which is shown in [44,49]:

$$\vec{F_L} = m_p \frac{2K\nu^{\frac{1}{2}} \rho d_{ij}}{\rho_p d_p (d_{lk} d_{kl})^{\frac{1}{4}}} (\vec{v} - \vec{v_p}) \tag{20}$$

where K is the Saffman number taken as K=2.594; and d_{ij} is the deformation tensor.

As tracking all nanoparticles individually is impractical and will involve a highly expensive simulation procedure, DPM divides similar nanoparticles into several small packs, and the position of each pack is determined by tracking a single representative nanoparticle. The number of packs is then determined by the meshes of the inlet of MCHS. In this study, the deposition rate is used to evaluate the nanoparticle deposition as:

$$\eta = \frac{N_d}{N_{total}} \times 100\% \tag{21}$$

where N_d is the number of nanoparticles deposited on the wall; and N_{total} is the total number of nanoparticles released from the inlet of the microchannel.

2.3. Thermophysical properties of nanofluids

Traditionally, heat transfer fluids such as water have a lower thermal conductivity than solids, so dispersing nano-sized solids such as alumina nanoparticles can enhance the thermophysical properties of the fluid. The thermophysical properties of nanoparticles are shown in Table 1, and the thermophysical properties of base fluids are shown in Table 2.

The thermophysical properties of nanofluids depend on the properties of nanoparticles, base fluid, temperature and nanoparticle concentration. The density ρ_{nf} and specific heat capacity $C_{p, nf}$ of nanofluid are

Table 1
Specific thermophysical properties of nanoparticles.

Thermophysical properties	Al$_2$O$_3$	Au	CNTs
ρ_p [kg/m^3]	3880	19,320	1600
$C_{p, p}$ [J/kgK]	733	129.81	687
k_p [W/mK]	36	297.73	2800

Table 2
Specific thermophysical properties of base fluids.

Thermophysical properties	Water	Methanol	Kerosene	Transformer oil
ρ_{bf} [kg/m³]	998.2	792	780	890
$C_{p, bf}$ [J/kgK]	4182	2226	2090	1860
k_{bf} [W/mK]	0.597	0.2	0.149	0.136
μ_{bf} [kg/ms]	0.000993	0.000544	0.0024	0.04361

determined by nanoparticle concentration φ and defined respectively as [50]:

$$\rho_{nf} = (1 - \varphi)\rho_{bf} + \varphi\rho_p \tag{22}$$

$$(\rho C_p)_{nf} = (1 - \varphi)(\rho C_p)_{bf} + \varphi(\rho C_p)_p \tag{23}$$

The dynamic viscosity μ_{nf} of water–alumina nanofluid is given as [51]:

$$\frac{\mu_{nf}}{\mu_{bf}} = exp\left(\frac{4.91\varphi}{0.2092 - \varphi}\right) \tag{24}$$

While the thermal conductivity k_{nf} of water–alumina nanofluid is shown as [52]:

$$\frac{k_{nf}}{k_{bf}} = 1 + 4.4Re_p^{0.4}Pr_{bf}^{0.66}\left(\frac{T}{T_{fr}}\right)^{10}\left(\frac{k_p}{k_{bf}}\right)^{0.03}\varphi^{0.66} \tag{25}$$

here, Re_p is the nanoparticles Reynolds number, defined as:

$$Re_p = \frac{\rho_{bf}v_Bd_p}{\mu_{bf}} = \frac{2\rho_{bf}k_bT}{\pi\mu_{bf}^2d_p} \tag{26}$$

where v_B is the nanoparticle Brownian velocity; T_{fr} is the freezing point of base fluid.

2.4. Simulation procedures

The DPM is used to solve the transport phenomena of nanofluids in the microchannel with the specific boundary conditions, as shown in Table 3. Various heat fluxes and velocities are selected to achieve the research aims. The inlet velocity ranges from 0.1 to 1 m/s, corresponding to the flow Reynolds numbers between 10.71 and 107.1. Since the simulation is intended to analyse nanoparticle deposition on walls, the near-wall grid density must be refined. Therefore, the dimensionless distance from the wall (y^+) is maintained at a value <1. At the same time, the meshing at the inlet section is also densified to resolve the stiff gradient near the inlet zone, as shown in Fig. 1. Due to the laminar flow and simple structure, the SIMPLE algorithm is introduced as a pressure-based solver coupling pressure and velocity in equations. The second-order central difference scheme is applied to the diffusion and convective terms of the transport equations. For all the governing equations performed in this simulation, converged solutions are usually achieved with the residuals <10^{-6}.

3. Grid sensitivity test and solution verification

In order to ensure the accuracy of the simulation results and grid

sensitivity, the average Nusselt number and deposition rate are calculated and shown in Table 4. In this case, the heat flux of 100 kW/m² is considered on the bottom wall of the MCHS, the inlet velocity is kept at 0.1 m/s (Re = 10.72), and the nanoparticle diameter is 10 nm. Five grid combinations are used: 15*50*1200, 20*65*1200, 25*75*1200, 25*75*1500 and 25*75*1800. It is shown that the average Nusselt numbers are unchanged from 25*75*1200, and the deviation of the deposition efficiency is only 0.07% for the grid numbers between 25*75*1200 and 25*75*1500. Therefore, the grid 25*75*1200 (giving the total number of mesh nodes 2,373,176) is deemed to be sufficient for the simulation, considering both the accuracy and computational cost.

Simultaneously, the simulation validation is performed for the flow field and nanoparticle deposition. As shown in Fig. 2, the Nusselt number is compared with the data published in the literature at different Reynolds numbers [40,53,54], and the results agree well. The changing trend of nanoparticle deposition in Fig. 3 is also in line with the simulation and theoretical results in the published papers [55,56]. It is worth noting that there is a small difference below 40 nm (maximum 0.25%) because this model induced Gaussian white noise (random signal) to calculate the Brownian motion in Eq. (9), and the Brownian effect increases with the decrease of nanoparticle diameter, as shown in Eq. (10). However, the trend remains the same, and the difference of 0.25% is also insignificant.

4. Results and discussion

A reduction in nanoparticle deposition is necessary to improve the stability of NF-MC. Thus, in order to determine the optimal working conditions for reducing deposition in cooling systems, DPM numerically analyses the nanofluid properties (i.e., nanoparticle diameter, nanoparticle density, base-fluid density and base-fluid viscosity) as well as the flow characteristics (i.e., velocity, heat flux, and inlet temperature). In addition, heat transfer performance and pressure drop are considered and the findings are presented in the sections below.

4.1. Influence of particle diameter

The bottom wall of the microchannel in this case is heated with a heat flux of 100 kW/m², whereas the remaining walls are kept adiabatic. The inlet temperature is 300 K, and the nanoparticle concentration is 1%. Fig. 4 illustrates that the nanoparticle deposition rate decreases with increasing nanoparticle diameter at different velocities. Brownian motion in this case is a dominant factor in the flow of nanoparticles [57]. For instance, as shown in Eqs. (9 and 10), when the nanoparticle diameter increases, the Brownian motion decreases, resulting in a longer radial-directional residence time for the nanoparticles in motion. Moreover, since the fluid velocity is kept the same, the axial-directional residence time remains nearly the same. The nanoparticles, therefore, spend more time travelling to the walls, which retards their deposition. Additionally, the thermophoresis and Saffman's lift forces also affect the nanoparticle deposition. As can be seen from Eq. (13), the thermophoresis force is proportional to the nanoparticle diameter, so more nanoparticles leave the hot surfaces with the increase of nanoparticle diameters. With the increase in nanoparticle diameter as in Eq. (20), the Saffman's lift force decreases, resulting in an increase in the radial-directional residence time, which in turn prolongs the deposition time

Table 3
Boundary conditions.

	Type	Heat Flux [kW/m²]	Velocity [m/s]	Pressure [Pa]	DPM	Other
Inlet	Velocity-Inlet	/	0.1–1	/	Escape	280 K, 290 K and 300 K fluid temperature
Outlet	Pressure-Outlet	/	/	0	Escape	/
Top Wall	Wall	0	/	/	Trap	No-slip boundary
Side Wall	Wall	0	/	/	Trap	No-slip boundary
Bottom Wall	Wall	20, 50 and 100	/	/	Trap	No-slip boundary

Table 4

Average Nusselt number and deposition rate at different grids.

Grid	15*50*1200	20*65*1200	25*75*1200	25*75*1500	25*75*1800
Nodes	980,016	1,664,586	2,373,176	2,965,976	3,375,000
$\overline{Nu}$	0.094795	0.0947687	0.0948398	0.094911	0.094968
η	10.4%	8.54%	8.43%	8.36%	8.32%
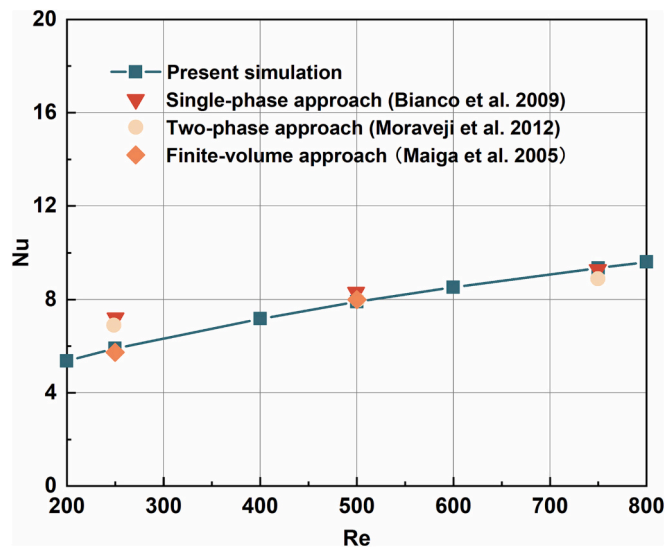
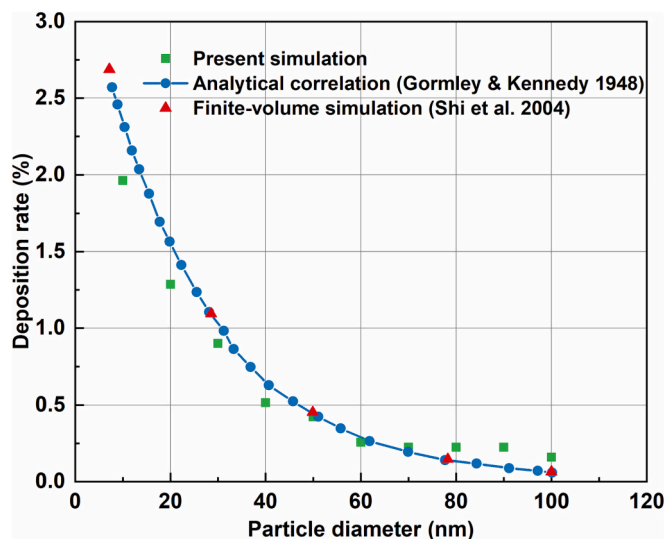**Fig. 2.** Nusselt number varies with Reynolds number in a nanoparticle concentration of 1%.

Fig. 3. Deposition rate changes with nanoparticle diameter.

in the same manner as Brownian motion. Other important forces, such as virtual mass and drag forces, are also affected by the nanoparticle movement track. Even though they are perpendicular to the deposition direction, the axial-directional residence time is affected. According to Eqs. (15) and (16), as the nanoparticle diameter increases, the virtual mass and drag forces increase as well, causing the nanoparticles to move rapidly in the axial direction. It is therefore indirectly possible to reduce the axial-directional residence time, thereby reducing the deposition rate.

Furthermore, the actual velocity needs to be considered when selecting the appropriate nanoparticle diameter for the MCHS systems

designed to reduce nanoparticle deposition. As further shown in Fig. 4, when the MCHS system requires a deposition rate lower than 1%, the nanoparticle diameters need to be >40 nm, 30 nm, 20 nm, 15 nm, and 15 nm, respectively for the fluid velocity of 0.2 m/s, 0.4 m/s, 0.6 m/s, 0.8 m/s, and 1 m/s. In order to reduce the nanoparticle deposition in MCHS, the nanoparticle diameter should not be too small, or the fluid velocity should be improved. In fact, the particle diameter does not always reduce the deposition rate. To further explore the influence of particle diameter on particle deposition, Fig. 5 illustrates a large range of particle diameters for the two selected velocities, 0.1 m/s and 0.2 m/s. The deposition rate drops initially, then stabilises until it increases rapidly when the particle diameter is above 3900 nm. The specific value depends on the velocity. This is because the gravitational force contributes significantly to deposition rates at diameters over 3900 nm. However, it must be noted that large-diameter particles are no longer suitable for microsystems [58]. From both these figures, it can therefore be concluded that the deposition rate of NF-MCs decreases as the nanoparticle diameter increases.

Furthermore, in addition to the nanoparticle deposition rate, heat transfer and pressure drop should also be considered when selecting the nanoparticle diameter of nanofluids. However, there are many controversial observations and conclusions reported in the literature regarding the effect of nanoparticle size [59–61], which require further investigation. Therefore, in Fig. 6, four major influence factors such as the nanoparticle deposition rate, the average heat transfer coefficient, the total nanoparticle surface area and the pressure drop are presented with nanoparticle diameters ranging from 10 nm to 50 nm at a velocity of 0.5 m/s. Based on the graph, increasing the diameter of nanoparticles results in a decrease in the pressure drop and deposition rate, thereby reducing the pump power and energy consumption. While the pressure drop is not pronounced when the nanoparticle diameter increases from 10 nm to 50 nm. The main reason for the increase in pressure drop by adding nanoparticles is the enhancement of the viscosity of nanofluid, which is only related to the nanoparticle concentration, not the diameter of nanoparticles. Thus, the pressure drop has negligible influence. However, the pressure drop is still reduced by only 0.02% due to an increase in the shear stress between nanofluid layers, as the nanoparticle diameter increases. Nevertheless, due to the small size of nanoparticles and their low concentrations, this influence is unlikely to have a significant impact.

In terms of heat transfer performance, as also shown in Fig. 6, the average heat transfer coefficient decreases from 14.91 kW/(m². K) to 14.75 kW/(m². K) as the nanoparticle diameter increases from 10 nm to 50 nm. This is due to three important reasons: firstly, large nanoparticles have a small surface-to-volume ratio resulting in a low thermal conductivity, thus nanoparticles with a smaller diameter exhibit a higher heat transfer coefficient; secondly, large nanoparticles reduce the Brownian motion, thus further reducing the chaotic movements of nanoparticles [62]; and finally, nanoparticle migration results in the loss of properties of nanofluids [63]. In spite of this, the heat transfer coefficient is not sensitive to nanoparticle diameters. This finding is in agreement with the experiment conducted by He et al. [64] and the simulation performed by Kalteh et al. [65]. More specifically, the heat transfer coefficient only reduces by 1.08% when the diameter of the nanoparticles increases from 10 to 50 nm, due to the slight difference in the surface area of the nanoparticles (based on Fig. 6, the total nanoparticle surface area decreases by 12.86 cm²).

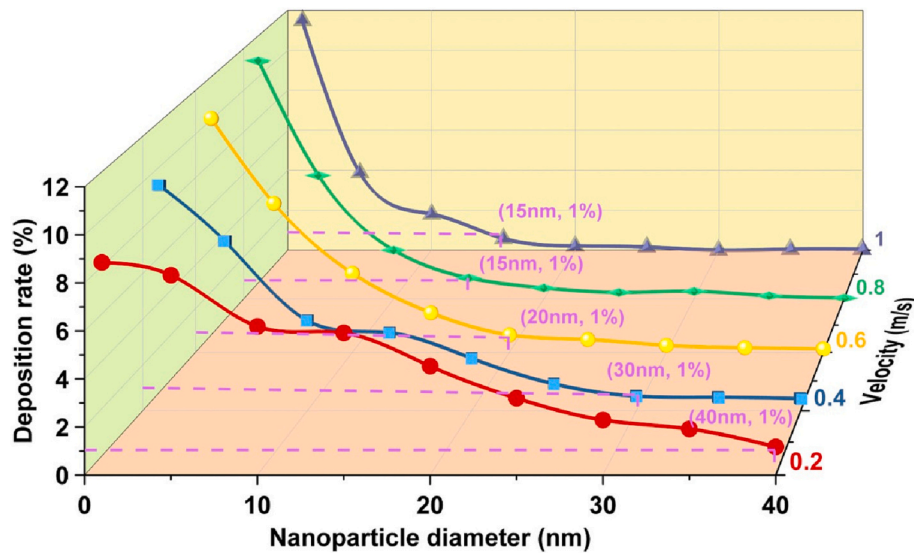The reduction in heat transfer caused by an increase in nanoparticle

Fig. 4. Deposition rate against the nanoparticle diameter at different velocities.
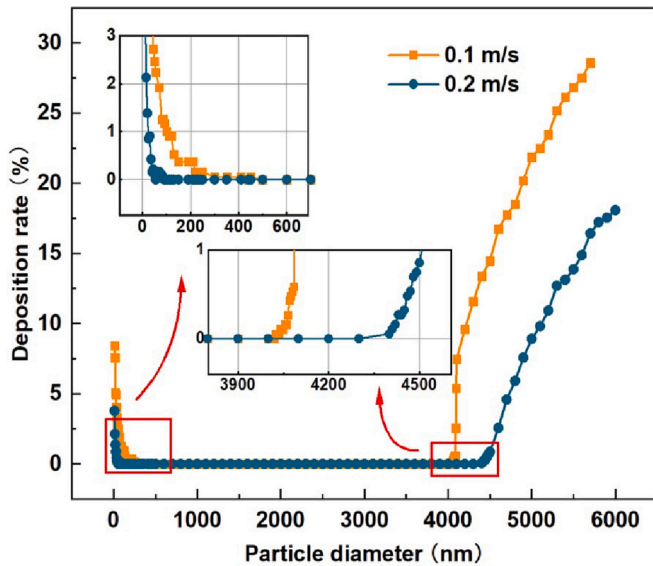

Fig. 5. Deposition rate varies with a large range of particle diameters.

diameter is also demonstrated in Fig. 7, where the local heat transfer coefficient along the MCHS for different nanoparticle diameters is presented. The heat transfer coefficient drops sharply from the inlet and then monotonically reduces in the flow direction due to the development of the thermal boundary layer and the increase of the nanofluid temperature [66]. The thermal boundary layer eventually plateaus to a constant in the fully developed region, keeping the heat transfer almost constant. Overall, heat transfer and pressure drop are only slightly affected by increasing nanoparticle diameters. It does, however, reduce the deposition rate, which may reduce corrosion and clogging of the MCHS, extending its lifetime.

4.2. Influence of density and viscosity of nanofluids

The selection of appropriate nanoparticles and base fluids for the synthesis of nanofluids can also reduce the number of depositions. Therefore, the highest and lowest thermophysical properties of frequently used nanoparticles and base fluids [10] are selected for the study. Tables 2 and 3 provide the details of these specific thermophysical

properties. As shown in Fig. 8, nanoparticle deposition can be alleviated by selecting high-density nanoparticles and low-density base fluids. In Fig. 8 (a), the deposition number is presented with the variation of the nanoparticle diameter at the highest or lowest density (Au and CNTs) with the base fluids of water and kerosene. The simulation boundary conditions, in this case, are as follows: the inlet temperature of 300 K, the nanoparticle concentration of 1%, the velocity of 0.2 m/s, and a heat flux of 100 kW/m^2 applied to the bottom wall of the microchannel. As shown in this figure, the deposition number of high-density nanoparticles (Au) is less than that of low-density nanoparticles (CNTs) at the same base fluids and nanoparticle diameters, while the deposition number of high-density base fluid (water) is much more than that of low-density base fluid (kerosene) at the same nanoparticles and nanoparticle diameters. The main reason is that the density of nanoparticles and base fluid affects the Brownian motion, the pressure gradient, and the Saffman's lift forces, and ρ_p/ρ is inversely proportional to these forces, as indicated by Eqs. (10), (19) and (20). Therefore, the decrease in ρ_p/ρ leads to a decrease in these forces, resulting in reduced deposition numbers.

As far as the influence of viscosity is concerned, only the viscosity of the base fluid has been studied since the addition of low-concentration nanoparticles leads to a slight change in the viscosity of nanofluids. As a consequence, it appears that a high-viscosity base fluid can prevent the nanoparticle deposition. Fig. 8 (b) illustrates that the deposition number varies according to the diameter of nanoparticles in the highest (transformer oil) and lowest (methanol) base fluids of commonly used nanofluids. The nanoparticles are Au. Based on the simulation of using transformer oil, the deposition number is virtually zero, far lower than the deposition number generated by using methanol. Therefore, it is understood that high-viscosity base fluids stabilise nanofluids due to their enhanced resistance to nanoparticle flow compared to low-viscosity base fluids.

4.3. Influence of velocity

Fig. 9 shows the changing trends in the deposition rate against the velocity and it is interesting to report the two distinct features – one of which is having the general trend of the deposition rate decreasing with the increasing velocity when the nanoparticle diameter exceeds 5 nm, while the other is opposite when the nanoparticle diameter is 1 nm. The former is due to the fact that both the Brownian motion and the thermophoresis force are unaffected by fluid velocity, so the radial-directional residence times remain almost the same. However, virtual
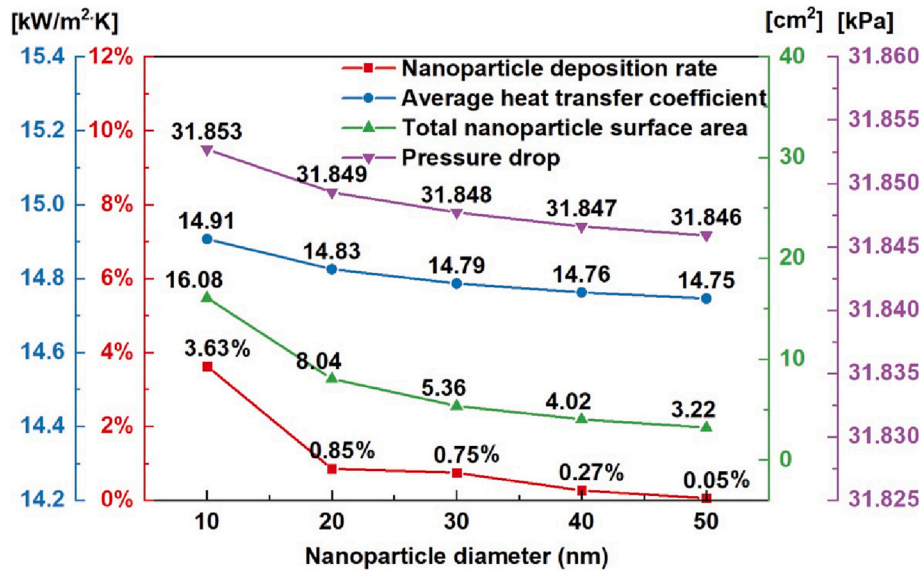
Fig. 6. Nanoparticle deposition rate, average heat transfer coefficient, total nanoparticle surface area and pressure drop change with nanoparticle diameters.
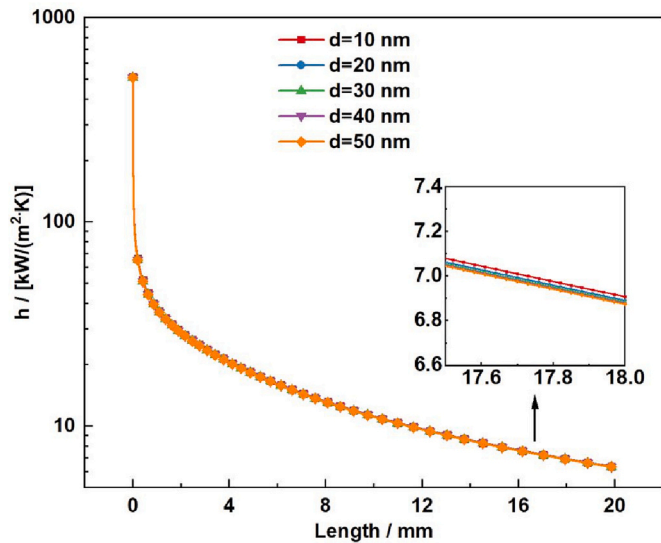

Fig. 7. The local heat transfer coefficient variation along the microchannel depending on the nanoparticle diameter.

mass and drag forces increase with the increase of velocity, resulting in a decrease in axial-directional residence time. Therefore, the nanoparticles require a considerable amount of time to deposit on the walls. In contrast, for the latter, as the velocity increases from 0.1 to 1 m/s for the nanoparticle diameter of 1 nm, the deposition rate is no longer sensitive to the velocity, even though a slight increase in the deposition number is predicted. In order to further investigate this phenomenon, a scaling analysis is performed as shown in Table 5. The scaling analysis of the y-direction forces (Brownian motion, thermophoretic force, gravity, pressure gradient force and Saffman's lift force) is calculated according to Eqs. (9), (12), (14), (19) and (20). It can be seen that the dominant forces are Brownian motion and the thermophoretic force when the diameter is above 10 nm [35], while Brownian motion and the Saffman's lift force become the main forces when the diameter is 1 nm. Brownian forces increase with decreasing diameter, and this force is not affected by velocity, so the trend is not sensitive to the velocity. However, the velocity does affects the Saffman's lift force. As shown in Eq. (20), increasing velocity and decreasing diameter strengthen this force,

thereby reducing the radial-directional residence time of nanoparticles. As reported in the section above, the axial-directional residence time is decreased simultaneously because of both the virtual mass and drag forces, but the radial-directional influence is more significant due to the micro-size channel. Therefore, the trend is a slight increase. It should be noted that the simulation boundary conditions, in this case, remain the same (i.e., inlet temperature 300 K, nanoparticle concentration 1%, and heat flux 100 kW/m^2).

For further understanding of this phenomenon and the pattern of nanoparticle deposition, Fig. 10 illustrates the specific deposition positions along the microchannel for various nanoparticle diameters and velocities. Table 6 shows specific working conditions. The 20 mm microchannel is divided into six segments, and due to the differences in surface areas between the six segments, the average number of depositions per unit area is calculated to evaluate the deposition situation. As can be seen, segment 1 has the highest deposition number, while the rest are almost identical. Most nanoparticles deposit in segment 1 because nanoparticles near the microchannel inlet are easy to deposit. With the nanofluid flowing, the majority of the nanoparticles migrate towards the centreline [67,68], which results in a decrease in depositions. In addition, the inlet effect also contributes to increased deposition as the unstable flow in the inlet section changes nanoparticle directions randomly. Upon reaching a fully developed state, the number of depositions becomes almost constant.

Furthermore, Fig. 11 shows the specific number of depositions on each wall. Since the side area differs from the top and bottom areas, it is necessary to calculate the average deposition number per unit area. As can be seen, the deposition numbers of the top and bottom walls are almost identical, and so are the deposition numbers of the two sides. The reason can be explained by the temperature and velocity magnitude contours of the cross-section in the midplane, as shown in Fig. 12. According to Fig. 12 (a), the temperature contour of the microchannel cross-section is asymmetric in the y-direction due to heating from the bottom wall. In contrast, the magnitude contour of velocity is symmetric in the y-direction, as can be seen in Fig. 12 (b). It is clear that the temperature has little effect on the fluid velocity contour in the microchannel because of its high velocity. In addition, the gravity of nanoparticles can also be ignored, while Brownian motion plays the greatest role in determining their moving directions. Thus, the deposition numbers at the top and bottom are similar. In regard to the walls of both sides, the velocity and temperature contours are symmetrical in the x-direction, so the deposition number is also the same on both sides. It is
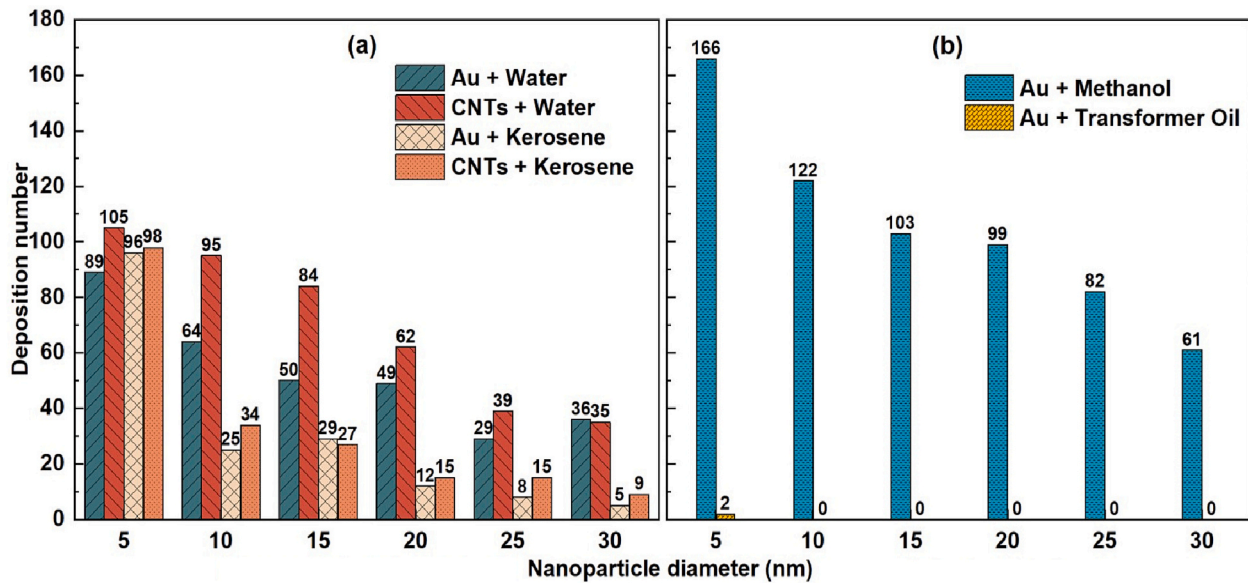
Fig. 8. Deposition number varies with the nanoparticle diameters in different nanoparticles and base fluids at the velocity of 0.2 m/s.
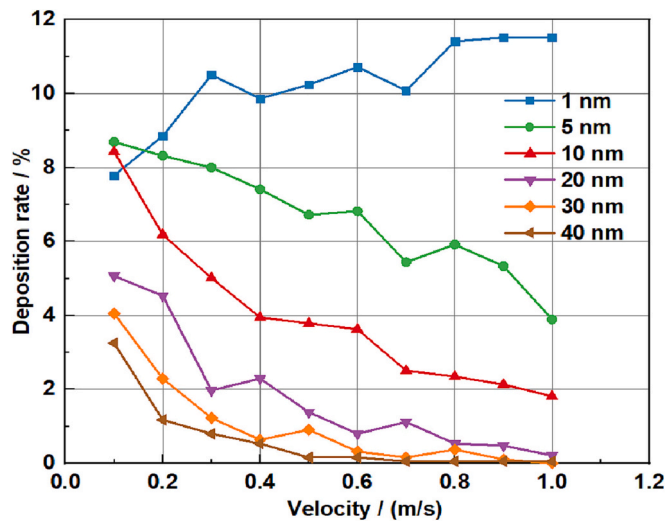

Fig. 9. The deposition rate varies with velocity in different nanoparticle diameters.

Table 5
Scaling analysis of five kinds of forces.

	1	2	3	4	5
$d_p = 1$ nm	$F_B \sim 10^{-13}$	$F_T \sim 10^{-19}$	$F_G \sim 10^{-20}$	$F_P \sim 10^{-23}$	$F_L \sim 10^{-17}$
$d_p = 10$ nm	$F_B \sim 10^{-15}$	$F_T \sim 10^{-18}$	$F_G \sim 10^{-20}$	$F_P \sim 10^{-23}$	$F_L \sim 10^{-18}$
$d_p = 100$ nm	$F_B \sim 10^{-17}$	$F_T \sim 10^{-17}$	$F_G \sim 10^{-20}$	$F_P \sim 10^{-23}$	$F_L \sim 10^{-19}$
Required scales	$\mu \sim 10^{-3}$, $k \sim 1$, $k_p \sim 10$, $K_n \sim 10^{-2}$, $\rho \sim 10^3$, $\rho_p \sim 10^3$, $d_{ij} \sim 10^{-2}$, $\vartheta \sim 10^{-6}$, $m_p \sim 10^{-21}$, $T \sim 10^2$, $\Delta T \sim 10$, $k_B \sim 10^{-23}$				

worth noting that the number of depositions on the top and bottom walls is more than those on the sides because only Brownian motion affects the nanoparticle deposition on the side walls. However, the gravity, thermophoresis, pressure gradient and Saffman's lift forces act vertically apart from Brownian motion. This causes the nanoparticle deposition on both the top and bottom walls.

The heat transfer and pressure drop are also affected by velocity, as shown in Fig. 13. Two different nanoparticle concentrations (1% and 4%) are considered in this case and the nanoparticle diameter is 10 nm.

It is shown that the deposition rate decreases along with the increase in nanoparticle concentration because the increased nanoparticles enhance the chance of collision with the walls. As for heat transfer performance, the average heat transfer coefficient increases as the velocity increases. The heat transfer enhancement is caused by the convective heat transfer coefficient being proportional to the thermal conductivity and inversely proportional to the thermal boundary layer thickness. Simultaneously, the decrease in velocity is accompanied by a decrease in the boundary layer thickness [64] and an increase in thermal conduction (dynamic effect) [69].

Moreover, the heat transfer coefficient improves slightly as the nanoparticle concentration increases at a given velocity. For example, when the nanofluid concentrations are 1% and 4% with a velocity of 1 m/s, the heat transfer coefficients are 16.83 kW/(m^2. K)and 17.56kW/(m^2. K), respectively. A clear demonstration of this phenomenon can be found in Fig. 14, which illustrates the local heat transfer coefficient for nanoparticle concentrations of 0%, 1% and 4% with velocities of 0.6 m/s and 1 m/s. Added the nanoparticle increases the local heat transfer coefficient, and this enhancement is more evident at a high fluid velocity. This is because nanoparticles improve thermal conduction, and the improvement increases as nanoparticle concentration increases. However, the viscosity of fluids also increases due to the increase in nanoparticles, resulting in an increase in boundary layer thickness [64]. It is also clear that the heat transfer coefficients are enhanced by the influence of thermal conduction over the fluid viscosity.

Nevertheless, the pressure drop increases with the increase of velocities, requiring more energy to promote the nanofluids and leading to an increase in energy consumption. At the same time, the pressure drop enhances as the nanoparticle concentrations increase due to the increase in the viscosity of the working fluid. As shown in Fig. 13, for example, at 1 m/s, when the nanofluid concentrations are 1% and 4%, the pressure drops are 68.448 kPa and 169.533 kPa, respectively. In summary, the increase in fluid velocity reduces the nanoparticle deposition and enhances heat transfer but must balance with the severe pressure drop.

4.4. Influence of heat flux

To investigate the influence of heat flux on NF-MCs, nanoparticle deposition rate, average heat transfer coefficient, and pressure drop are simulated at heat fluxes ranging from 20 kW/m^2 to 100 kW/m^2, as shown in Fig. 15. The nanoparticle diameter, in this case, is 10 nm, the inlet temperature is 300 K, the velocity is 0.6 m/s, and the nanoparticle
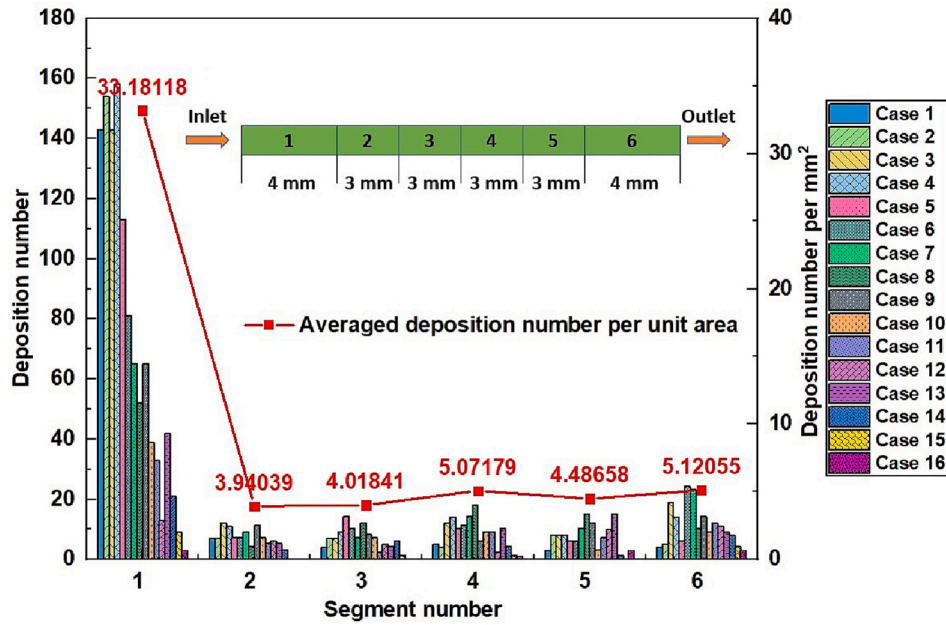
Fig. 10. The local deposition at each segment of microchannel for various nanoparticle diameters and velocities.

Table 6
The simulation conditions at various diameters and velocities.

	Case 1	Case 2	Case 3	Case 4	Case 5	Case 6	Case 7	Case 8
d (nm)	1	1	1	1	5	5	5	5
v (m/s)	0.2	0.4	0.6	0.8	0.2	0.4	0.6	0.8
	Case 9	Case 10	Case 11	Case 12	Case 13	Case 14	Case 15	Case 16
d (nm)	10	10	10	10	20	20	20	20
v (m/s)	0.2	0.4	0.6	0.8	0.2	0.4	0.6	0.8

concentration is 1%. Increasing the heat flux from 20 kW/m² to 100 kW/m², the nanoparticle deposition rate increases slightly from 2.51% to 2.72% due to Brownian motion and thermophoresis force. On the one hand, the nanofluid temperature is affected by the heat flux in the microchannel. The high heat flux results in a high average fluid temperature, and an increased fluid temperature enhances Brownian motion, aggravating nanoparticle irregular movement according to Eqs. (9) and (10). As a result, nanoparticles are more likely to move close to walls. On the other hand, heat flux also affects fluid temperature differences. According to Fig. 16, the centreline temperature of the bottom wall and midplane varies with the different heat fluxes along the microchannel, and the fluid velocity at the inlet is 0.6 m/s. In the same cross-section, the higher the heat flux, the greater the temperature difference between the bottom wall and midplane. In addition, Eq. (12)
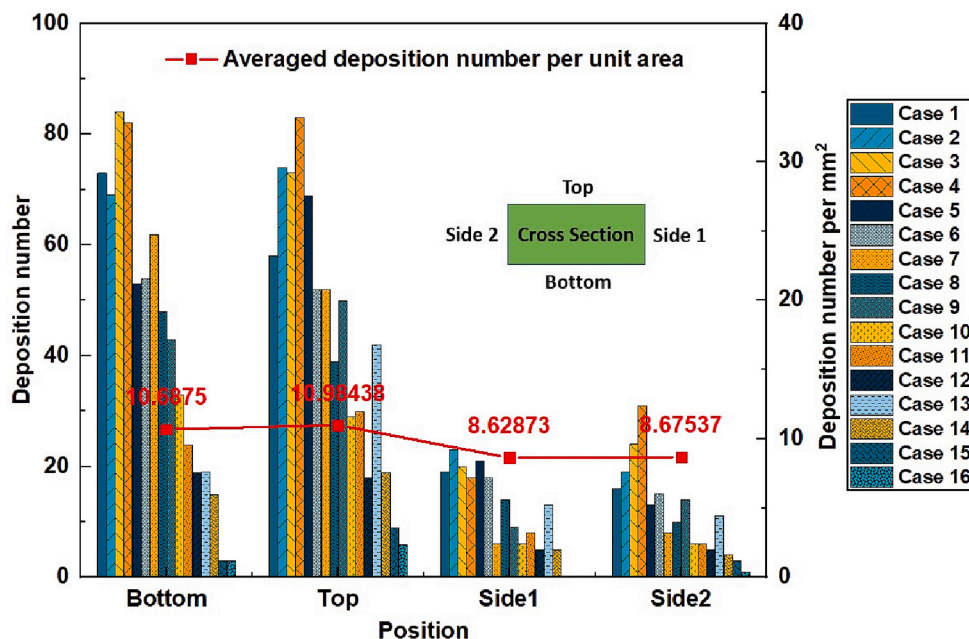

Fig. 11. The local deposition at each wall of microchannel for various nanoparticle diameters and velocities.
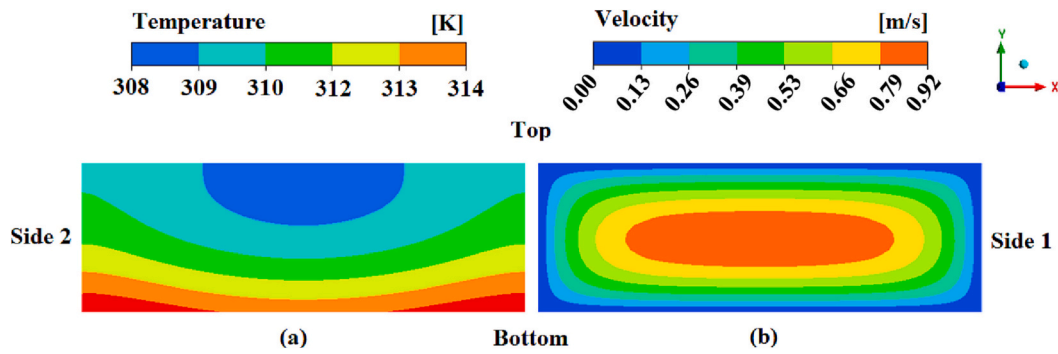
Fig. 12. Contour of the cross section in the midplane at a fluid velocity of 0.5 m/s: (a) temperature contour and (b) velocity magnitude contour.
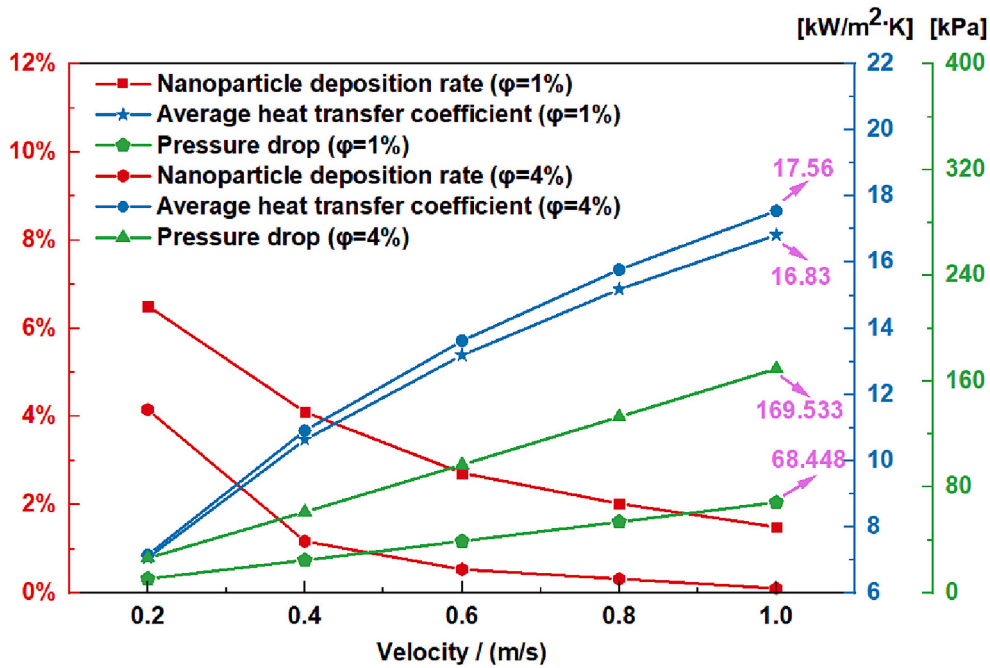

Fig. 13. Nanoparticle deposition rate, average heat transfer coefficient and pressure drop change with the velocity at the nanoparticle concentrations of 1% and 4%.
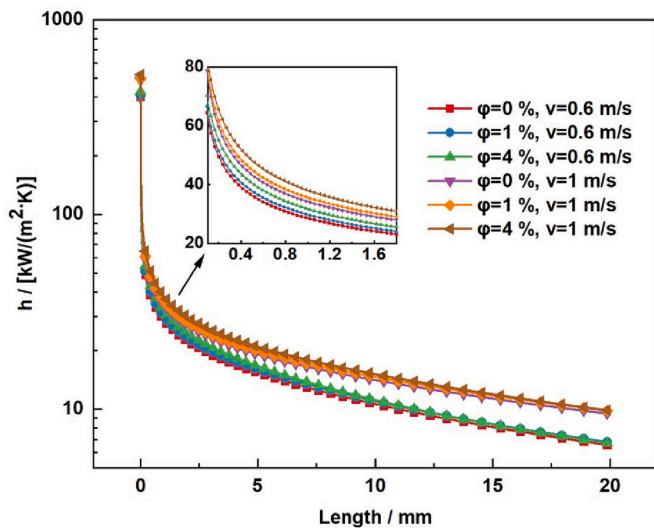

Fig. 14. The local heat transfer coefficient varies along the microchannel for different nanoparticle concentrations and velocities.

indicates that the temperature difference increases the thermophoresis force, forcing nanoparticles to move from hot to cold areas. As a result, nanoparticles are less likely to reach the wall. Despite the opposing effects of Brownian motion and thermophoresis force, the Brownian motion is stronger than thermophoresis. Therefore, the deposition rate increases slightly. Furthermore, the average heat transfer coefficient only increases by 0.92%, while the pressure drop decreases by 10.57% due to the decrease in nanofluid viscosity. Overall, the heat transfer coefficient and the nanoparticle deposition rate are not significantly affected by the increase in heat flux, while the pressure drop decreases.

4.5. Influence of inlet temperature

Inlet temperature also affects the heat transfer performance of the microchannel. As shown in Fig. 17, the nanoparticle deposition rate, average heat transfer coefficient, and pressure drop change with the inlet temperature, which has been set at 280 K, 290 K, and 300 K to prevent boiling at the outlet. In this case, the nanoparticle diameter is 10 nm, the velocity is 0.6 m/s, the heat flux is 100 kW/m^2, and the nanoparticle concentration is 1%. Increasing the inlet temperature from 280 K to 300 K increases the deposition rate from 0.80% to 2.72%, because the inlet temperature has a significant impact on the fluid temperature. As shown in Fig. 18, the centreline temperature changes
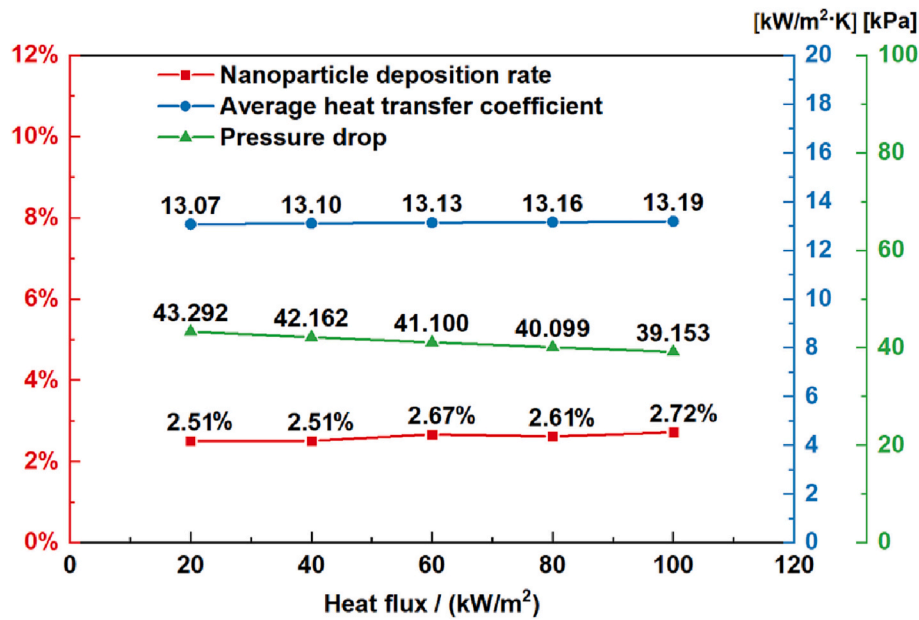
Fig. 15. Nanoparticle deposition rate, average heat transfer coefficient and pressure drop change with the heat flux.
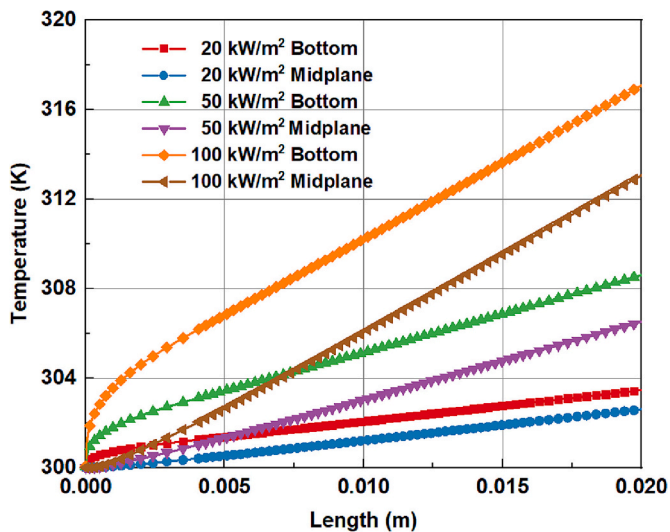

Fig. 16. Temperature changes with the length of the microchannel for the bottom wall and midplane centreline.

along the channel. As the inlet temperature increases, the average fluid temperature increases, so the Brownian motion also enhances according to Eqs. (9) and (10). Thus, a low inlet temperature reduces the deposition rate effectively below the boiling point.

Moreover, a decrease in the inlet temperature has a negative effect on the average heat transfer coefficient, but the reduction is not pronounced, only decreasing by 2.73% when the inlet temperature is reduced from 300 K to 280 K. However, by decreasing the inlet temperature from 300 K to 280 K, the pressure drop does increase by 60.21% simultaneously. This is because a decrease in temperature increases nanofluid viscosity, which results in increased pressure drop. Therefore, decreasing the inlet temperature leads to a substantial pressure drop, which is not an excellent option for reducing nanoparticle deposition.

5. Conclusions

To determine the optimal working conditions for reducing deposition in NF-MC cooling systems, several important factors were examined by DPM. Several significant findings are reported as below:

- When the nanoparticles were increased from 10 nm to 50 nm, the average heat transfer coefficient decreased only by 1.08%, and the pressure drop decreased only by 0.02%. By increasing the nanoparticle diameters, the deposition rate was effectively reduced while the pressure drop and heat transfer coefficient remained largely unchanged.
- Choosing high-density nanoparticles, low-density base fluids and high-viscosity base fluids reduced the deposition numbers.
- When the fluid velocity increased from 0.2 m/s to 1 m/s, the nanoparticle deposition rate decreased from 6.51% to 1.49%, the average heat transfer coefficient increased from 7.06 kW/(m^2. K) to 16.83 kW/(m^2. K), and the pressure enhanced from 10.743 kPa to 68.448 kPa. The appropriate velocity should be therefore selected according to specific NF-MC systems.
- Changing heat flux was not an ideal way to reduce nanoparticle deposition.
- Finally, when the inlet temperature increased from 280 K to 300 K, the average deposition rate increased from 0.80% to 2.72%. In contrast, the average heat transfer rate only reduced by 2.73% and the pressure drop increased by 60.21%. Thus, it is important to balance the pressure drop and nanoparticle deposition when designing a NF-MC system.

CRediT authorship contribution statement

Meng Wang: Conceptualization, Methodology, Software, Validation, Investigation, Formal analysis, Visualization, Writing – original draft, Writing – review & editing. **Phillip S. Dobson:** Conceptualization, Supervision, Writing – review & editing, Resources. **Manosh C. Paul:** Conceptualization, Supervision, Writing – review & editing, Project administration, Resources, Funding acquisition.
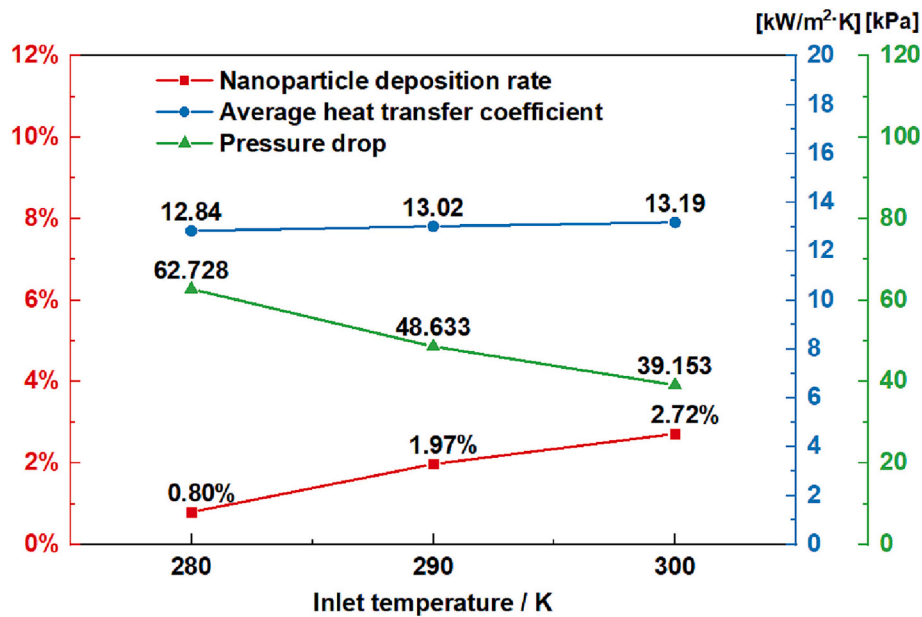
Fig. 17. Nanoparticle deposition rate, average heat transfer coefficient and pressure drop change with the inlet temperature.
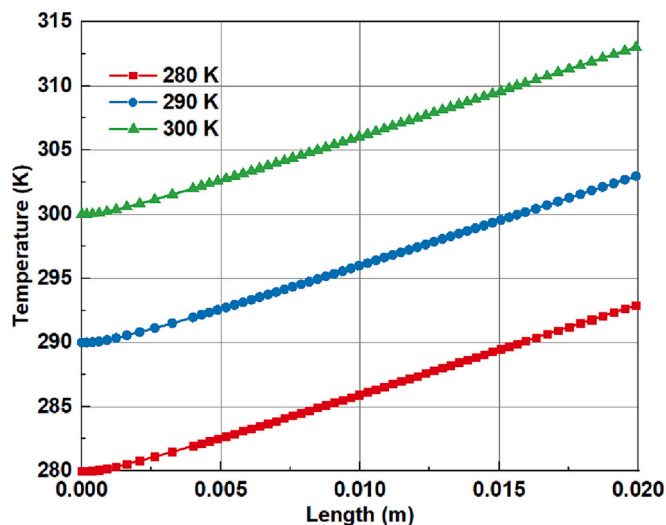

Fig. 18. Temperature changes with the length of the microchannel for the midplane centreline.

Declaration of Competing Interest

The authors declare the following financial interests/personal relationships which may be considered as potential competing interests:

Meng Wang reports financial support was provided by China Scholarship Council with the University of Glasgow.

Data availability

Data will be made available on request.

References

[1] S.U. Choi, J.A. Eastman, Enhancing Thermal Conductivity of Fluids with Nanoparticles, Argonne National Lab, IL (United States), 1995.

[2] T.J. Choi, B. Subedi, H.J. Ham, M.S. Park, S.P. Jang, A review of the internal forced convective heat transfer characteristics of nanofluids: experimental features, mechanisms and thermal performance criteria, J. Mech. Sci. Technol. 32 (8) (2018) 3491–3505.

[3] S.M. AlDosari, S. Banawas, H.S. Ghafour, I. Tlili, Q.H. Le, Drug release using nanoparticles in the cancer cells on 2-D materials in order to target drug delivery: a numerical simulation via molecular dynamics method, Eng. Analys. Bound. Elem. 148 (2023) 34–40.

[4] M. Dehghan, M. Daneshipour, M.S. Valipour, Nanofluids and converging flow passages: a synergetic conjugate-heat-transfer enhancement of micro heat sinks, Int. Commun. Heat Mass Transf. 97 (2018) 72–77.

[5] D. Wen, Y. Ding, Experimental investigation into convective heat transfer of nanofluids at the entrance region under laminar flow conditions, Int. J. Heat Mass Transf. 47 (24) (2004) 5181–5188.

[6] M.H. Esfe, S. Saedodin, M. Mahmoodi, Experimental studies on the convective heat transfer performance and thermophysical properties of MgO–water nanofluid under turbulent flow, Exp. Thermal Fluid Sci. 52 (2014) 68–78.

[7] A.S.M. Aljaloud, L. Manai, I. Tlili, Bioconvection flow of cross nanofluid due to cylinder with activation energy and second order slip features, Case Stud. Therm. Eng. 42 (2023), 102767.

[8] J. Bai, D.H. Kadir, M.A. Fagiry, I. Tlili, Numerical analysis and two-phase modeling of water graphene oxide nanofluid flow in the riser condensing tubes of the solar collector heat exchanger, Sustain. Energy Technol. Assessm. 53 (2022), 102408.

[9] N.H. Naqiuddin, L.H. Saw, M.C. Yew, F. Yusof, T.C. Ng, M.K. Yew, Overview of micro-channel design for high heat flux application, Renew. Sust. Energ. Rev. 82 (2018) 901–914.

[10] M.U. Sajid, H.M. Ali, Thermal conductivity of hybrid nanofluids: a critical review, Int. J. Heat Mass Transf. 126 (2018) 211–234.

[11] S. Chakraborty, P.K. Panigrahi, Stability of nanofluid: a review, Appl. Therm. Eng. 174 (2020), 115259.

[12] D.B. Tuckerman, R.F.W. Pease, High-performance heat sinking for VLSI, IEEE Electron Dev. Lett. 2 (5) (1981) 126–129.

[13] J.A. Khan, A.M. Morshed, R. Fang, Towards ultra-compact high heat flux microchannel heat sink, Proc. Eng. 90 (2014) 11–24.

[14] C.A. Rubio-Jimenez, A. Hernandez-Guerrero, J.G. Cervantes, D. Lorenzini-Gutierrez, C.U. Gonzalez-Valle, CFD study of constructal microchannel networks for liquid-cooling of electronic devices, Appl. Therm. Eng. 95 (2016) 374–381.

[15] Z. He, Y. Yan, Z. Zhang, Thermal management and temperature uniformity enhancement of electronic devices by micro heat sinks: a review, Energy 216 (2021) 119223.

[16] M. Dehghan, M. Daneshipour, M.S. Valipour, R. Rafee, S. Saedodin, Enhancing heat transfer in microchannel heat sinks using converging flow passages, Energy Convers. Manag. 92 (2015) 244–250.

[17] H. Wang, Z. Chen, J. Gao, Influence of geometric parameters on flow and heat transfer performance of micro-channel heat sinks, Appl. Therm. Eng. 107 (2016) 870–879.

[18] M. Mirzaei, M. Dehghan, Investigation of flow and heat transfer of nanofluid in microchannel with variable property approach, Heat Mass Transf. 49 (2013) 1803–1811.

[19] M. Abd-Elhady, C. Rindt, A. Van Steenhoven, Optimization of flow direction to minimize particulate fouling of heat exchangers, Heat Transf. Eng. 30 (10−11) (2009) 895–902.

[20] H. Müller-Steinhagen, M. Malayeri, A. Watkinson, Heat exchanger fouling: mitigation and cleaning strategies, Heat Transf. Eng. 32 (2011) 189–196.

[21] E. Davoudi, B. Vaferi, Applying artificial neural networks for systematic estimation of degree of fouling in heat exchangers, Chem. Eng. Res. Des. 130 (2018) 138–153.

[22] X. Wei, L. Wang, Synthesis and thermal conductivity of microfluidic copper nanofluids, Particuology. 8 (3) (2010) 262–271.

[23] X. Li, D. Zhu, X. Wang, Evaluation on dispersion behavior of the aqueous copper nano-suspensions, J. Colloid Interface Sci. 310 (2) (2007) 456–463.

[24] B. Munkhbayar, M.J. Nine, J. Jeoun, M. Bat-Erdene, H. Chung, H. Jeong, Influence of dry and wet ball milling on dispersion characteristics of the multi-walled carbon nanotubes in aqueous solution with and without surfactant, Powder Technol. 234 (2013) 132–140.

[25] X. Li, D. Zhu, X. Wang, N. Wang, J. Gao, H. Li, Thermal conductivity enhancement dependent pH and chemical surfactant for Cu-H2O nanofluids, Thermochim. Acta 469 (1–2) (2008) 98–103.

[26] K.-Y. Kwak, C.-Y. Kim, Viscosity and thermal conductivity of copper oxide nanofluid dispersed in ethylene glycol, Korea-Austr. Rheol. J. 17 (2) (2005) 35–40.

[27] M. Kole, T. Dey, Effect of prolonged ultrasonication on the thermal conductivity of ZnO–ethylene glycol nanofluids, Thermochim. Acta 535 (2012) 58–65.

[28] W. Duangthongsuk, S. Wongwises, Comparison of the effects of measured and computed thermophysical properties of nanofluids on heat transfer performance, Exp. Thermal Fluid Sci. 34 (5) (2010) 616–624.

[29] D. Wen, L. Zhang, Y. He, Flow and migration of nanoparticle in a single channel, Heat Mass Transf. 45 (8) (2009) 1061–1067.

[30] C. Fang, T. Ou, X. Wang, M. Rui, W. Chu, Effects of feed solution characteristics and membrane fouling on the removal of THMs by UF/NF/RO membranes, Chemosphere. 260 (2020), 127625.

[31] C.Y. Tang, T. Chong, A.G. Fane, Colloidal interactions and fouling of NF and RO membranes: a review, Adv. Colloid Interf. Sci. 164 (1–2) (2011) 126–143.

[32] A. Giacobbo, J.M. do Prado, A. Meneguzzi, A.M. Bernardes, M.N. de Pinho, Microfiltration for the recovery of polyphenols from winery effluents, Sep. Purif. Technol. 143 (2015) 12–18.

[33] Y. El Rayess, C. Albasi, P. Bacchin, P. Taillandier, J. Raynal, J. Mietton-Peuchot, et al., Cross-flow microfiltration applied to oenology: a review, J. Membr. Sci. 382 (1–2) (2011) 1–19.

[34] Y. Cheng, H. Chen, Z. Zhu, T. Jen, Y. Peng, Experimental study on the anti-fouling effects of Ni–Cu–P-PTFE deposit surface of heat exchangers, Appl. Therm. Eng. 68 (1–2) (2014) 20–25.

[35] S. Goudarzi, M. Shekaramiz, A. Omidvar, E. Golab, A. Karimipour, A. Karimipour, Nanoparticles migration due to thermophoresis and Brownian motion and its impact on Ag-MgO/water hybrid nanofluid natural convection, Powder Technol. 375 (2020) 493–503.

[36] F. Hedayati, G. Domairry, Effects of nanoparticle migration and asymmetric heating on mixed convection of TiO2–H2O nanofluid inside a vertical microchannel, Powder Technol. 272 (2015) 250–259.

[37] D.-B. Kwak, S.C. Kim, H. Lee, D.Y. Pui, Numerical investigation of nanoparticle deposition location and pattern on a sharp-bent tube wall, Int. J. Heat Mass Transf. 164 (2021), 120534.

[38] F. Bao, H. Hao, Z. Yin, C. Tu, Numerical study of nanoparticle deposition in a gaseous microchannel under the influence of various forces, Micromachines. 12 (1) (2021) 47.

[39] Z.-Q. Yin, X.-F. Li, F.-B. Bao, C.-X. Tu, X.-Y. Gao, Thermophoresis and Brownian motion effects on nanoparticle deposition inside a 90 square bend tube, Aerosol Air Qual. Res. 18 (7) (2018) 1746–1755.

[40] M.K. Moraveji, E. Esmaeili, Comparison between single-phase and two-phases CFD modeling of laminar forced convection flow of nanofluids in a circular tube under constant heat flux, Int. Commun. Heat Mass Transf. 39 (8) (2012) 1297–1302.

[41] S.K. Das, S.U. Choi, W. Yu, T. Pradeep, Nanofluids: Science and Technology, John Wiley & Sons, 2007.

[42] ANSYS I, ANSYS FLUENT Release 2021 R1, Theory Guide Canonsburg, PA, 2021.

[43] W.C. Hinds, Aerosol Technology: Properties, Behavior, and Measurement of Airborne Particles, John Wiley & Sons, 1999.

[44] A. Li, G. Ahmadi, Dispersion and deposition of spherical particles from point sources in a turbulent channel flow, Aerosol Sci. Technol. 16 (4) (1992) 209–226.

[45] J. Rostami, A. Abbassi, Conjugate heat transfer in a wavy microchannel using nanofluid by two-phase Eulerian–Lagrangian method, Adv. Powder Technol. 27 (1) (2016) 9–18.

[46] L. Talbot, Thermophoresis of particles in a heated boundary layer, J. Fluid Mech. 101 (4) (1979) 737–758.

[47] A.H. Sulaymon, C.A. Wilson, A.I. Alwared, Experimental determination of the virtual mass coefficient for two spheres accelerating in a power law fluid, J. Fluids Eng. 132 (12) (2010).

[48] A. Gosman, E. Loannides, Aspects of computer simulation of liquid-fueled combustors, J. Energy. 7 (6) (1983) 482–490.

[49] P. Saffman, The lift on a small sphere in a slow shear flow, J. Fluid Mech. 22 (2) (1965) 385–400.

[50] Y. Xuan, W. Roetzel, Conceptions for heat transfer correlation of nanofluids, Int. J. Heat Mass Transf. 43 (19) (2000) 3701–3707.

[51] W. Williams, J. Buongiorno, L.-W. Hu, Experimental investigation of turbulent convective heat transfer and pressure loss of alumina/water and zirconia/water nanoparticle colloids (nanofluids) in horizontal tubes, J. Heat Transf. 130 (4) (2008).

[52] M. Corcione, Empirical correlating equations for predicting the effective thermal conductivity and dynamic viscosity of nanofluids, Energy Convers. Manag. 52 (1) (2011) 789–793.

[53] S.E.B. Maiga, S.J. Palm, C.T. Nguyen, G. Roy, N. Galanis, Heat transfer enhancement by using nanofluids in forced convection flows, Int. J. Heat Fluid Flow 26 (4) (2005) 530–546.

[54] V. Bianco, F. Chiacchio, O. Manca, S. Nardini, Numerical investigation of nanofluids forced convection in circular tubes, Appl. Therm. Eng. 29 (17–18) (2009) 3632–3642.

[55] H. Shi, C. Kleinstreuer, Z. Zhang, C. Kim, Nanoparticle transport and deposition in bifurcating tubes with different inlet conditions, Phys. Fluids 16 (7) (2004) 2199–2213.

[56] P. Gormley, M. Kennedy, Diffusion from a stream flowing through a cylindrical tube, in: Conference Diffusion from a Stream Flowing through a Cylindrical Tube vol. 52, JSTOR, 2023, pp. 163–169.

[57] M. Wang, M.C. Paul, P. Dobson, Influence of Brownian Motion on Nanoparticle Deposition in a Microchannel Heat Sink, 2021.

[58] L.H. Kumar, S. Kazi, H. Masjuki, M. Zubir, A review of recent advances in green nanofluids and their application in thermal systems, Chem. Eng. J. 429 (2022), 132321.

[59] C.T. Nguyen, G. Roy, C. Gauthier, N. Galanis, Heat transfer enhancement using Al2O3–water nanofluid for an electronic liquid cooling system, Appl. Therm. Eng. 27 (8–9) (2007) 1501–1506.

[60] D.P. Kulkarni, P.K. Namburu, H. Ed Bargar, D.K. Das, Convective heat transfer and fluid dynamic characteristics of SiO2 ethylene glycol/water nanofluid, Heat Transf. Eng. 29 (12) (2008) 1027–1035.

[61] R.S. Vajjha, D.K. Das, D.P. Kulkarni, Development of new correlations for convective heat transfer and friction factor in turbulent regime for nanofluids, Int. J. Heat Mass Transf. 53 (21−22) (2010) 4607–4618.

[62] D. Kim, Y. Kwon, Y. Cho, C. Li, S. Cheong, Y. Hwang, et al., Convective heat transfer characteristics of nanofluids under laminar and turbulent flow conditions, Curr. Appl. Phys. 9 (2) (2009) e119–e123.

[63] K. Anoop, T. Sundararajan, S.K. Das, Effect of particle size on the convective heat transfer in nanofluid in the developing region, Int. J. Heat Mass Transf. 52 (9–10) (2009) 2189–2195.

[64] Y. He, Y. Jin, H. Chen, Y. Ding, D. Cang, H. Lu, Heat transfer and flow behaviour of aqueous suspensions of TiO2 nanoparticles (nanofluids) flowing upward through a vertical pipe, Int. J. Heat Mass Transf. 50 (11−12) (2007) 2272–2281.

[65] M. Kalteh, A. Abbassi, M. Saffar-Avval, J. Harting, Eulerian–Eulerian two-phase numerical simulation of nanofluid laminar forced convection in a microchannel, Int. J. Heat Fluid Flow 32 (1) (2011) 107–116.

[66] P. Eneren, Y.T. Aksoy, M.R. Vetrano, Experiments on single-phase Nanofluid heat transfer mechanisms in microchannel heat sinks: A review, Energies. 15 (7) (2022) 2525.

[67] A. Malvandi, D. Ganji, Effects of nanoparticle migration on force convection of alumina/water nanofluid in a cooled parallel-plate channel, Adv. Powder Technol. 25 (4) (2014) 1369–1375.

[68] M. Bahiraei, Particle migration in nanofluids: a critical review, Int. J. Therm. Sci. 109 (2016) 90–113.

[69] C.W. Sohn, M. Chen, Microconvective Thermal Conductivity in Disperse Two-Phase Mixtures as Observed in a Low Velocity Couette Flow Experiment, 1981.